

## Demonstration of a radio-frequency spectrum analyser based on spectral hole burning

IVAN LORGERÉ, LOÏC MÉNAGER, VINCENT LAVIELLE,  
JEAN-LOUIS LE GOUËT, DANIEL DOLFI, SYLVIE TONDA  
and JEAN-PIERRE HUIGNARD

Laboratoire Aimé Cotton, CNRS II, bâtiment 505, 91405 Orsay  
Cedex, France; Thales, Laboratoire Central de Recherche, Domaine de  
Corbeville, 91404 Orsay Cedex, France

*(Received 15 February 2002; revision received 10 May 2002)*

**Abstract.** We demonstrate application of spectral hole burning to the spectral analysis of broad-band rf signals. In quite the same way as an acousto-optic spectrometer, the device operates on an optically carried rf signal and achieves angular separation of the signal spectral components. An instantaneous bandwidth of 2.5 GHz has been achieved, with a power dynamic range of 35 dB, limited by the detector. Extension to greater than 10 GHz instantaneous bandwidth with greater than 1000 channels is consistent with the active material capabilities.

### 1. Introduction

One employs heterodyne receivers in many applications when a signal is analysed with high spectral resolution. In (sub)millimetre astronomy the input signal is processed by the low noise ‘front-end’ of the system, which includes mixing and amplification stages, before being conveyed to the spectrometer. The most widely used spectrometers in radio astronomy are the acousto-optic spectrometer, autocorrelation spectrometer and the filter-bank spectrometer. Spectrometers based on all types of technology, except the autocorrelation type, must be designed with fixed bandwidth and resolution, that is they are inflexible for different kinds of observation. The autocorrelation spectrometer is in this regard flexible but can suffer from a comparably high power consumption when processing broad bandwidths. To be able to process very wide bandwidth signals (1–4 GHz), most spectrometers must use a prefiltering stage to reduce the broad signal band into several narrower subbands, thus using a hybrid technique. The bandwidth of the filters can be 1–1.5 GHz for the acousto-optic spectrometer and 0.2–1 GHz for the autocorrelation spectrometer.

We present the first laboratory demonstration of a large bandwidth rf spectrometer, based on the spectral-hole-burning (SHB) process. This work continues a preliminary study that we recently published [1]. We expect to outdo the bandwidth of the acousto-optic spectrometer and autocorrelation spectrometer by a factor of better than ten, exceeding 10 GHz. As an optoelectronic system, the SHB spectrometer would feature consumption requirements similar to those of the

acousto-optic spectrometer. It would exhibit the additional benefit of resolution and bandwidth flexibility.

The price to pay for these attractive properties is the cooling to an operating temperature of about 5 K. However, low-temperature operation should not be regarded as a major inconvenience. The launching of the ISO satellite, with a 2000 l tank of superfluid helium, recently demonstrated that large-scale extreme cryogenic conditions could be achieved in embarked experiments. This is confirmed by the forthcoming Planck and Herschel missions, where some devices are cooled down to 0.1 K.

Efforts to promote SHB technology were focused for a long time on large capacity data storage applications, thus masking the spectral specificity of the SHB process. Confronted with dominant conventional storage techniques, these efforts proved unsuccessful. The SHB technology is more likely to emerge in the field of optical processing since it offers outstanding performance in terms of bandwidth and time-bandwidth product. Various optical functions, such as time-domain correlation [2, 3], real-time data routing [4, 5] and true-time delay generation for radar application [6], have been demonstrated recently that illustrate SHB signal-processing potential. However, cryogenic requirements drastically limit the domains where a SHB solution is practicable. We believe that we have disclosed such an application field where the potential and demand for the device are both strong, where cryogenic requirements can be handled and where SHB solutions clearly outdo more conventional techniques.

## 2. Spectral-hole-burning spectrometer

### 2.1. Spectrometer concept

Owing to the broad bandwidth capabilities of optoelectronic components, it is worthwhile to process rf signal in the optical domain, after transfer on an optical carrier. This is the way that the SHB spectrometer operates. The concept relies on the engraving of monochromatic gratings in a SHB material. Each grating is able to diffract a single spectral component, with a resolution ultimately determined by the homogeneous linewidth of the SHB medium, which is usually less than 1 MHz at a temperature of 5 K. A large number of gratings can coexist within the inhomogeneous width of the absorption line, which may reach tens of gigahertz. By varying the laser frequency in synchronism with the angle of incidence during the engraving procedure, one associates a specific diffraction angle with each specific spectral component. Therefore, the different spectral components of an incident polychromatic probe beam are diffracted and simultaneously retrieved in different directions. The stack of monochromatic gratings works as a spectrometer which is expected to exhibit a resolution of less than 1 MHz and a bandwidth of several tens of gigahertz.

As depicted in figure 1, rf spectral analysis can be performed after transfer of the investigated microwave signal on an optical carrier with the help of a Mach-Zehnder electro-optic modulator. By fortunate coincidence, the bandwidth of the SHB medium indeed matches that of integrated Mach-Zehnder electro-optic modulator developed for high-flow telecommunication. The connection between the engraving incidence angle and laser frequency is essentially arbitrary. Therefore, reducing the engraving laser frequency scanning range while the angular

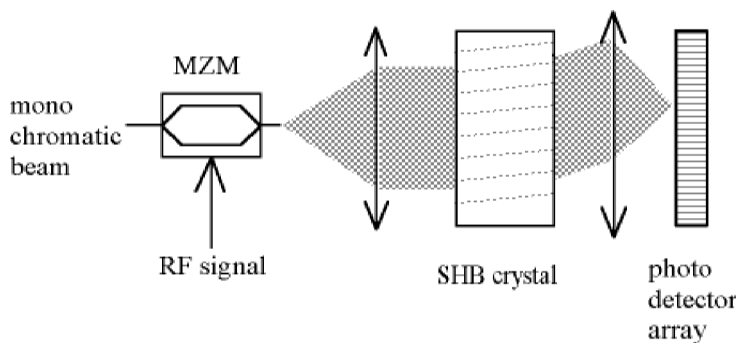


Figure 1. SHB spectrometer concept. The rf signal to be analysed is transferred on an optical carrier with the help of an integrated broad-band Mach-Zehnder electro-optic modulator. The angular separation of the side-band spectral components is effected by the gratings engraved in the SHB crystal.

scanning range is kept fixed, one actually zooms on a specific spectral region which is analysed with improved spectral resolution.

This design is reminiscent of the well-known acousto-optic spectrometer. In the latter device a Bragg cell achieves two functions. On the one hand, it transfers the rf signal on the optical carrier. On the other hand, it accomplishes the angular separation of the optically carried spectral components. The acoustic wave absorption limits the bandwidth to about 1 GHz. The integrated Mach-Zehnder electro-optic modulator offers a much larger bandwidth, in excess of 50 GHz, but it does half the job. It transfers the rf signal on the optical carrier but does not achieve the angular separation of the spectral components, since the carrier and the side bands propagate along the same direction. In the SHB spectrometer, the SHB crystal is intended to complement the Mach-Zehnder electro-optic modulator component by achieving the missing angular separation.

## 2.2. Spectral-hole-burning engraving

When guest absorbing centres are embedded in a solid state host matrix, their absorption spectrum is broadened by the matrix defects and disorder. This is known as inhomogeneous broadening. When the temperature is lowered to a few kelvins, the inhomogeneous width does not change significantly while the spectral width of the individual active centre is dramatically reduced [7]. The width of an individual spectral line is said to be 'homogeneous' and is denoted as  $\Gamma_h$ . At 5 K, this quantity may be  $10^3$ – $10^6$  times narrower than the inhomogeneous width  $\Gamma_{inh}$ . When the material is illuminated by a monochromatic laser at frequency  $\nu_L$ , only the active centres that are resonant with the light source are optically excited (figure 2). Their selective radiative excitation leads to the burning of a hole  $2\Gamma_h$  wide at frequency  $\nu_L$  in the absorption band profile. This spectrally selective process is known as 'spectral hole burning'. In a simple system, active centres rapidly return to their initial ground state and the spectral hole is erased. However, phototransformation channels may be opened by the optical excitation. Then the final state of the system differs from its initial ground state and the burnt hole may survive for hours or days at low temperatures. One can meet all intermediate situations, from transient holes of nanosecond lifetime, to permanent holes.

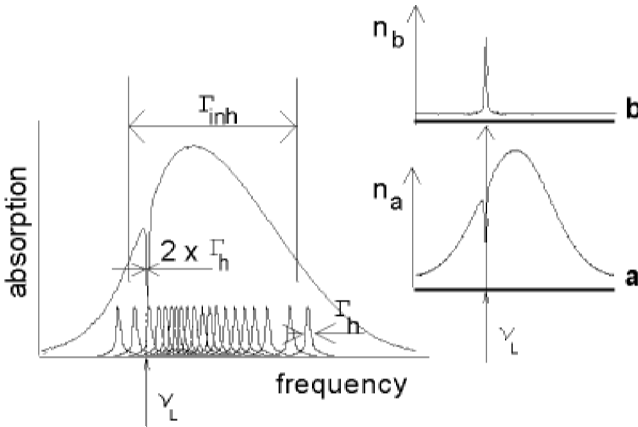


Figure 2. Monochromatic excitation of a SHB material. The atom individual absorption lines  $\Gamma_h$  wide are distributed over a frequency interval  $\Gamma_{inh}$  wide. The laser selectively excites atoms at frequency  $\nu_L$ . The resulting population transfer from ground state 'a' to excited state 'b' is reflected in a hole that is burnt in the inhomogeneously broadened absorption profile.

The hole depth depends on the energy dose delivered by the monochromatic laser at the burning position. When two coherent beams are directed to the material, the spatial energy distribution of the burning light is determined by the interference pattern of the beams. Therefore, an absorption Bragg grating is drawn throughout the illuminated sample volume by the spatial distribution of SHB. The crucial point is that the grating only exists at the very wavelength of the burning light. When tuned to the burning wavelength, a probe beam undergoes diffraction. It no longer meets any grating as soon as its frequency differs from the burning frequency by more than  $2\Gamma_h$ . Since one grating only spans a spectral interval  $2\Gamma_h$  wide, and since the available spectral domain is given by  $\Gamma_{inh}$ , one concludes that  $\Gamma_{inh}/2\Gamma_h$  independent gratings can be hosted at the same spatial location. Hole-burning spectral selectivity is local in essence and strongly differs from conventional Bragg selectivity. The latter occurs in holograms engraved by counterpropagating beams and depends on the sample thickness.

It should be stressed that, unlike holograms recorded in a photorefractive material, the gratings engraved at different wavelengths in a SHB medium do not share the maximum available diffraction efficiency: each one is built from active centres that are all resonant at one and only one specific wavelength. Therefore one should not observe the familiar  $1/N^2$  diffraction efficiency decay that results from the multiplexing of  $N$  gratings in a photorefractive material.

### 2.3. Spectral-hole-burning material: rare-earth-ion-doped crystals

Rare-earth ion-doped crystals represent a satisfactory candidate for high-resolution applications. The common structure of rare-earth atoms is  $5s^2 5p^6 4f^{n+1} 6s^2$ , where  $0 \leq n \leq 13$ . In triply charged ions, one  $4f$  electron and both  $6s$  electrons are removed. Optical transitions within the  $4f^n$  configuration are forbidden for parity reasons. Nevertheless some weak lines, with oscillator strength of the order of  $10^{-8}$ , result from mixing with the  $4f^{(n-1)} 5d$  configuration in sites without inversion symmetry. In addition the sharpness of the lines is

preserved, in a solid state matrix, by the shielding of 4f electrons by the 5s and 5p electrons. At 5 K in a crystal host matrix the homogeneous linewidth is usually much smaller than 1 MHz. If profitable as far as spectral resolution is concerned, a weak oscillator strength unfortunately means that a larger amount of energy is needed for engraving.

On some transitions the ions behave as two-level atoms, with an excited state that directly decays to the ground state. Then the spectral hole lifetime coincides with that of the excited state. The  ${}^4I_{13/2} \rightarrow {}^4I_{15/2}$  transition of  $\text{Er}^{3+}$  near  $1.5 \mu\text{m}$  belongs to this class. It offers a 10 ms storage time in the upper level [8]. Different processes may slow down the return to initial state and the spontaneous erasure of the engraved structure. In  $\text{Eu}^{3+}$ -doped crystals, resonant excitation results in an optical pumping alteration of the atom distribution over the ground-state hyperfine structure [9]. This alteration may survive for hours before return to thermal equilibrium. The long memory life is obtained at the expense of the bandwidth. Indeed the lines connected to the different hyperfine sublevels overlap, which limits the available bandwidth to a few gigahertz.

On the  ${}^2H_4 \rightarrow {}^2H_6$  transition in  $\text{Tm}^{3+}$ -doped crystals, a bottleneck metastable state, with a lifetime of about 10 ms, delays the excited state decay to the ground state [10]. This is the ion that we elected as the active material in our project (figure 3). The  ${}^3H_4 \rightarrow {}^3H_6$  transition wavelength at 793 nm is compatible with integrated electro-optic  $\text{LiNbO}_3$  ultrafast modulators. This wavelength also falls within the range of common semiconductor lasers and of the titanium-sapphire laser. Optical pumping from the ground state to the bottleneck state  ${}^3F_4$  via the upper state  ${}^3H_6$  offers a convenient way to accumulate engraving [11]. Owing to the  $500 \mu\text{s}$  lifetime of the upper level, an optical pumping cycle lasts about 1 ms. Several cycles can take place during the 10 ms lifetime of  ${}^3F_4$ . We experimentally verified that a large fraction of the ground-state population can actually be transferred to  ${}^3F_4$ . This procedure entails two benefits. Firstly, optimal engraving can be reached without saturating the  ${}^3H_4 \rightarrow {}^3H_6$  transition, which means lower laser intensity requirements. Secondly, with a 1 kHz refresh rate and a 10 ms storage lifetime, the diffraction efficiency is nearly stationary.

Erbium-doped crystals in the  $1.5 \mu\text{m}$  range offers a very attractive alternative that we plan to consider in a future work but that we have not mastered yet. This

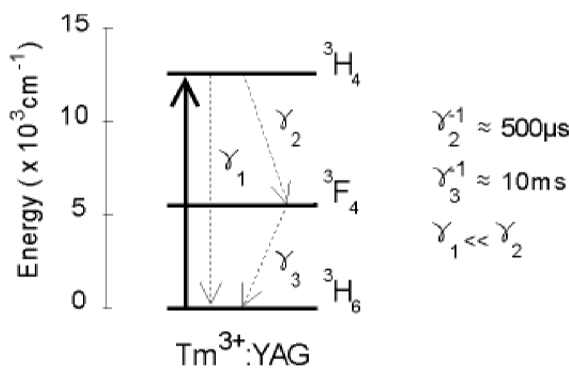


Figure 3. Level scheme in  $\text{Tm}^{3+}$ : yttrium aluminium garnet. Coupling with the laser is effected on the transition  ${}^3H_4 \rightarrow {}^3H_6$  at 793 nm. The level decay rates are denoted by  $\gamma_i$ .

choice should give access to the wealth of tools that has been developed for fibre-optics communications, including versatile lasers and amplifiers [5].

#### 2.4. Beam configuration

The beam configuration is strongly constrained by the material limitations. Owing to the short lifetime of the engraving, the gratings must be refreshed continuously and simultaneously diffract the impinging signal beam. This condition is satisfied in the ‘box configuration’ presented in figure 4. The probe beam that carries the rf signal to be processed propagates along  $\mathbf{k}_3$ . It lies out of the plane defined by the engraving beam wave-vectors  $\mathbf{k}_1$  and  $\mathbf{k}_2$ . This non-coplanar arrangement is consistent with simultaneous writing and readout since the diffracted beam is directed along  $\mathbf{k}_3 + \mathbf{k}_1 - \mathbf{k}_2$ , which differs from all the incident wave-vectors. The wave-vectors  $\mathbf{k}_2$  and  $\mathbf{k}_3$  are headed in fixed directions while  $\mathbf{k}_1$  rotates in synchronism with the frequency scan of the engraving beams. Therefore the different spectral components that are carried by the probe beam are diffracted in different directions. The wave-vector  $\mathbf{k}_1$  actually undergoes a two-dimensional raster motion, describing parallel lines in synchrony with the laser spectral scan. As illustrated in figure 4,  $\mathbf{k}_3$  is directed in such a way that the diffracted beam directions are interlaced with the engraving directions. This interlaced configuration minimizes phase mismatching.

#### 2.5. Spectral resolution; channel number

Let the engraving and probe beams exhibit the same Gaussian intensity profile and let  $w$  represent the diameter (full width at half-maximum (FWHM)) of this profile inside the SHB slab. When monochromatic, the probe beam is diffracted by the engraved grating in a specific frequency-dependent direction with the diffraction-limited angular resolution:

$$\delta\varphi = \frac{0.76\lambda}{w}, \quad (1)$$

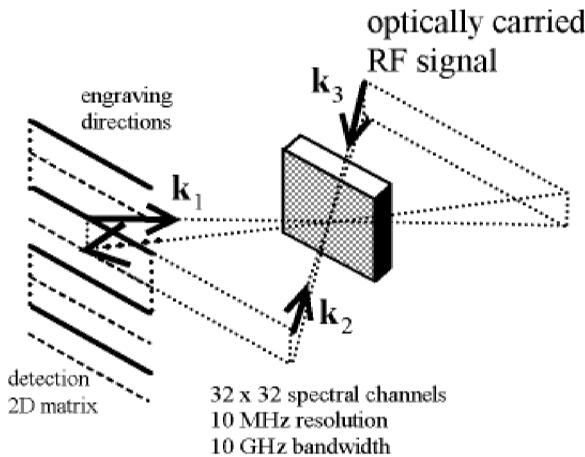


Figure 4. Counterpropagating box configuration with simultaneous engraving and readout. The diffracted signal directions are interlaced with the angular scan of engraving beam 1.

where  $\delta\varphi$  is the angular FWHM of the diffracted beam intensity. Let  $\bar{\varphi}$  denote the angular range of the rotating engraving beam in both space directions. Let  $N_x = \bar{\varphi}/\delta\varphi$  be the number of lines scrutinized by this beam during the frequency scan  $\bar{\nu}$  of the laser. Let  $N_y = \bar{\varphi}/\delta\varphi$  be the number of distinguishable points per line. Then the spectral channel number  $N = N_x N_y$  and the spectral resolution  $\delta\nu = \bar{\nu}/N$  are given by

$$N = 1.7 \left( \frac{\bar{\varphi}w}{\lambda} \right)^2 \quad \text{and} \quad \delta\nu = 0.58\bar{\nu} \left( \frac{\bar{\varphi}w}{\lambda} \right)^{-2} \quad (2)$$

respectively. One reaches 1000 channels with  $w = 230 \mu\text{m}$ ,  $\bar{\varphi} = 90 \text{mrad}$  and  $\lambda = 800 \text{nm}$ .

### 2.6. Photon echo configuration

In the above description of the SHB spectrometer concept we have considered that the engraving laser output is split into two chirped-frequency monochromatic beams, their angle of incidence on the active material being scanned in synchrony with their common optical frequency. In the present section we show that the spectral resolution of such a spectrometer would not reach the diffraction limit given by equations (1) and (2). To reach this limit the spectrometer must operate in the photon echo configuration.

Let  $E(\nu_0)$  represent the spectral amplitude of the incident probe field at frequency  $\nu_0$ . This field gives rise to a diffracted signal  $S(\nu_0, \nu)$ , not only in the direction associated with  $\nu_0$ , but also in directions associated with other frequencies  $\nu$  according to the following expression:

$$S(\nu_0, \nu) \propto E(\nu_0)F(\nu_0, \nu), \quad (3)$$

where the apparatus function  $F(\nu_0, \nu)$  is given by

$$F(\nu_0, \nu) = \int d\nu' \int_0^\infty d\tau [n(\nu' - \nu) \otimes L(\nu' - \nu)] \exp[2i\pi(\nu' - \nu_0)\tau - \Gamma_h\tau], \quad (4)$$

$$n(\nu) = \exp \left\{ - \left[ \left( \frac{2\nu}{\delta\nu} \right)^2 \ln 2 \right] \right\} \quad \text{and} \quad L(\nu) = \frac{1}{\pi} \frac{\Gamma_h/2\pi}{\nu^2 + (\Gamma_h/2\pi)^2}. \quad (5)$$

In equation 4, the convolution product is the spectral filter engraved in the crystal, for the spectral channel centred at frequency  $\nu$ . The convolution of the function  $n(\nu)$  conveyed by the engraving beams with the crystal homogeneous line shape  $L(\nu)$  is the result of the limited spectral resolution of the material. This spectral filter gives the fraction of the ions of resonant frequency  $\nu'$  which contribute to the diffraction in the direction associated with  $\nu$ . These ions excited at time  $-\tau$  by the probe field generate a coherent signal of frequency  $\nu'$  which decays at the rate  $\Gamma_h$ . The apparatus function is the sum of the ion response over the excitation time and the ion frequency. The causal character of the response is expressed by the lower boundary of the sum over the excitation time [12].

If the lower boundary of the integral over  $\tau$  were shifted to  $-\infty$ , equation 4 would reduce to

$$F(\nu_0, \nu) = n(\nu_0 - \nu) \otimes (L(\nu_0 - \nu) \otimes L(\nu_0 - \nu)), \quad (6)$$

which, under the assumption of narrow homogeneous width, would be consistent with the expected spectral resolution, as discussed in section 2.5. As expected, the homogeneous line shape comes into play twice: once at engraving and once at reading. This is the reason why the minimum hole width is twice the homogeneous linewidth in hole-burning experiments. Unfortunately one has to deal with the integral boundary at zero, which expresses the material response causality.

One readily arranges equation (4) in the following form:

$$F(\nu_0, \nu) = \frac{1}{2}n(\nu_0 - \nu) \otimes L(\nu_0 - \nu) \otimes L(\nu_0 - \nu) + \frac{i}{2\pi} \int d\nu' \frac{\nu_0 - \nu'}{(\nu_0 - \nu')^2 + (\Gamma_h/\pi)^2} n(\nu' - \nu). \tag{7}$$

The first term exhibits the resonant character of the absorption grating component, while the second term corresponds to the non-resonant dispersive grating component. However, it is possible to make the apparatus function recover the resonant shape depicted by equation (6). Let  $n(\nu)$  be modulated in the following way:

$$n(\nu) = \exp \left[ - \left( \frac{2\nu}{\delta\nu} \right)^2 \ln 2 + 2i\pi\nu t_{12} \right], \tag{8}$$

where the time parameter  $t_{12}$  satisfies the condition  $\delta\nu t_{12} > 1$ . In order to modulate  $n(\nu)$ , one just needs to maintain a constant frequency shift  $\Delta$  between the two engraving beams. In this configuration,  $t_{12}$  represents the time delay that separates the interactions of a specific frequency class of atoms with the two engraving beams. In the same way, the atomic response is delayed with respect to the interaction with the probe beam, behaving as a ‘photon echo’. The time delay  $t_{12}$  can be expressed as  $t_{12} = \Delta/r$ , where  $r$  stands for the engraving laser chirp rate. Then the second term in equation (7) takes on a resonant character and brings the same contribution as the first term. This turns out to entail important consequences as illustrated in figure 5 where the squared apparatus function  $|F(\nu_0, \nu)|^2$

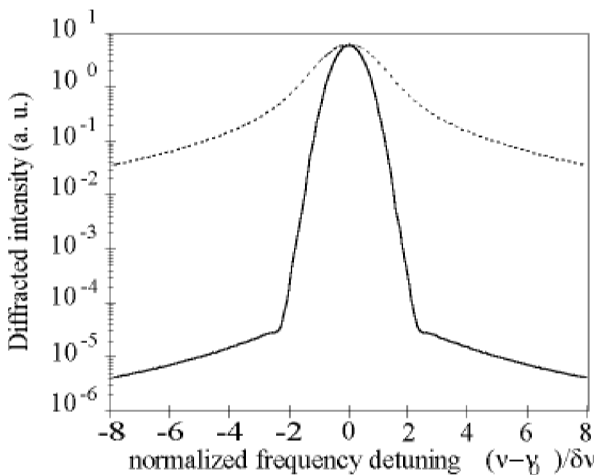


Figure 5. Diffracted intensity as a function of the frequency detuning  $\nu_0 - \nu$  for two values of the delay  $t_{12}$ : ( $\cdots$ ),  $t_{12} = 0$ ; (—),  $2\pi\delta\nu t_{12} = 5$ . The spectrometer resolution  $\delta\nu$  is set equal to ten times the homogeneous width:  $2\pi\delta\nu = 10\Gamma_h$ .

is displayed as a function of  $\nu_0 - \nu$  for  $t_{12} = 0$  and  $2\pi \delta\nu t_{12} = 5$ , with  $2\pi \delta\nu = 10\Gamma_h$ . The figure shows that delaying the second engraving beam by less than  $1/\delta\nu$  is enough to improve the cross-talk by more than 50 dB, with respect to the simultaneous engraving configuration, at a distance of  $2 \delta\nu$  from the spectral channel centre. In order to be engraved in the SHB material absorption profile, the spectral modulation period  $1/t_{12}$  has to be much larger than the material resolution  $\Gamma_h$ . Should this condition be violated, the diffracted intensity would decline according to the factor  $\exp(-4\Gamma_h t_{12})$ . Since the condition  $\delta\nu t_{12} > 1$  must be satisfied simultaneously, the diffraction efficiency is lowered as one makes the spectrometer channel width approach the ultimate material resolution  $\Gamma_h$ .

### 2.7. *Optically carried signal*

The rf signal to be analysed is transferred on the probe beam with the help of an integrated Mach-Zehnder electro-optic modulator. The notion of ‘carrier wave’ must be re-examined in the context of the SHB spectrometer. This notion applies to a signal whose field amplitude is given by

$$S(t) = \cos(\omega t) + \sum_{n=1}^N m_n \cos[(\omega + \Omega_n)t] + \sum_{n=1}^N m'_n \cos[(\omega - \Omega_n)t], \quad (9)$$

where frequencies  $\omega$  and  $\Omega_n$  respectively belong to the optical carrier and to the rf signal spectral components. The component weight factors are denoted  $m_n$ . This signal includes a carrier and two side bands. The signal is usually transmitted to a quadratic detector, with a bandwidth much smaller than the optical carrier frequency. The detector only sees the beat of each  $m_n$  spectral component against the carrier, averaged over many optical periods. In the absence of carrier the detector would collect an inextricable beat spectrum including components at  $\Omega_n \pm \Omega_n'$ . The present situation strongly differs from that narrow-band scheme because the SHB spectrometer is *able to identify the optical frequency itself*. As a consequence the carrier is useless at the detection stage. The relative spectral position of the programming and probe lasers can be chosen so that a single side band of the optically carried signal falls within the engraved filter range, the carrier itself being eliminated. This corresponds to zero-point carrier modulation conditions. Then the expression for the signal is

$$S(t) = \sum_{n=1}^N m_n \cos[(\omega + \Omega_n)t]. \quad (10)$$

Each spectral channel only detects the relevant *optical* frequency component  $\omega + \Omega_n$ . This has dramatic implications in terms of noise, background and sensitivity. Indeed the energy to be directed to the engraved gratings strictly reduces to the significant signal components. The carrier does not reach the cryostat windows or the crystal plate, which eliminates an important source of stray light. In addition the signal intensity on the engraved gratings can be enlarged within the limits imposed by the mixer of the rf source and the optical carrier. This should be contrasted with the acousto-optical spectrum analyser device where a Bragg cell achieves the angular separation of the rf signal spectral components. Then the optical carrier is mixed with the rf signal in the Bragg cell itself so that one cannot avoid the fact that the carrier coexists with the modulated side band inside the deflecting crystal.

### 3. Experimental set-up

In this first demonstration the spectral analysis is carried out along a single space dimension, with the help of a one-dimension photodiode array. The three beams are split from a single laser source.

In the engraving stage the angular scan is achieved by a frequency-shift-compensated pair of acousto-optic deflectors that are crossed successively by beam 1. The deflectors respectively diffract the light beam in order  $-1$  and  $+1$  so that the respective frequency downshift and upshift cancel each other when both devices are driven at the same frequency. The two deflectors are oriented in perpendicular directions and are slanted at  $45^\circ$  from horizontal. When the two deflectors are driven in synchrony, the emerging beam is scanned horizontally without any frequency shift. The angular scanning range is 86 mrad. With  $w = 180 \mu\text{m}$ , the expected diffraction-limited angular FWHM turns out to be about 3.4 mrad, which leads to a channel number of about 25.

The laser is swept in synchrony with the writing beam angular scan. This scan must be repeated over the spectrometer bandwidth with precision better than the desired resolution, since the grating storage is accumulated in the active crystal for several engraving cycles. Narrow-linewidth extended-cavity diode lasers with diffraction gratings have been developed for atomic spectroscopy applications. Commercially available devices can be tuned over several nanometres without mode hopping. The broad-range tuning usually involves motors for moving the grating. This well-controlled movement is necessarily slow. Smaller scans, over several tens of gigahertz, can be achieved with piezoelectric mounts and can therefore be cycled at rates as high as several hundreds of hertz. However, such fast scans suffer from hysteresis and from a lack of reproducibility. The repeatability requirements of our application forced us to develop a novel electro-optically tuned extended-cavity diode laser [13, 14].

A 100% duty cycle or interception rate can be attained only if engraving and readout work simultaneously. Two different lasers are needed to accomplish these two tasks since the engraving laser frequency is continuously scanned at fixed rate, while the rf signal to be investigated must be transferred on to a fixed frequency carrier. With a single laser in our arrangement, we are forced to operate in a sequenced mode, where grating engraving and signal diffraction are alternate. Engraving takes place during the first half-repetition-period, while the laser frequency is kept fixed for readout during the second half-period. The repetition rate of the writing-readout sequence is set at  $2000 \text{ s}^{-1}$ . The interval  $500 \mu\text{s}$  long defined by the trigger includes a writing step  $250 \mu\text{s}$  long, followed by a step of the same duration devoted to rf signal spectral analysis. Since the shelving state lifetime is about 10 ms, engraving is accumulated over about 20 writing steps.

In the first demonstration, we did not use a Mach-Zehnder modulator to transfer a rf signal on the probe beam. Instead we simulated multiple-line rf signals by making the laser perform various discrete frequency jumps during the readout step of the writing-readout sequence. Recent experiments, to be reported later, with a Mach-Zehnder modulator, showed that this simulation was relevant. The modulated probe beam is directed to the  $\text{Tm}^{3+}$ : yttrium aluminium garnet crystal and is diffracted on the engraved gratings into a frequency-dependent direction. The diffracted signal crosses a converging lens and is detected on a photodiode array (PDA) located in the focal plane. The PDA includes 1024 pixels. The pixels are 2.5 mm high and  $25 \mu\text{m}$  wide. They are sequentially read out every

10 ms. Since the detector is continuously operating this interval also represents the integration time. The illuminated position coordinate on the PDA is proportional to the deflection angle and also to the rf signal frequency. Without further improvement the PDA collects the stray light scattered on the cryostat windows. In order to filter out this unwanted background, we image the active region of the sample on a pinhole with the help of an optical relay. In this way the emitting area is precisely located. This procedure appears to be very efficient for the rejection of the stray light produced by the engraving beams.

## 4. Experimental results

### 4.1. Synchronized angle and frequency scans: stability, repeatability and spectral resolution

The angular distribution of a single line signal gives information on the accumulated engraving procedure with synchronized angle and frequency scans. Indeed let us direct a monochromatic pulse on the engraved crystal. The pulse is diffracted by the atoms with which it interacts resonantly. Any fluctuation in the connection between angle and frequency during the accumulated engraving process 10ms long will cause angular broadening of the diffracted signal. Such fluctuation may result either from laser instability or from any defect in the synchronized laser tuning and deflector driving. In the absence of fluctuation the angular FWHM of the diffracted beam will equal the diffraction limit given by equation (1). The main experimental values are summarized in table 1.

In a first experiment the engraving beams are swept over a 125 MHz interval with a chirp rate  $r = 500 \text{ GHz s}^{-1}$ . A rectangular probe pulse  $5 \mu\text{s}$  long is shaped by an acoustic-optic modulator placed on the probe beam. The diffracted signal is displayed in figure 6. The 86 mrad scanning range covers a 516 pixel interval on the photodiode array. The diffraction-limited width predicted from the values listed in table 1 is  $\delta\varphi = 3.4 \text{ mrad}$ . A more precise value is derived from the direct analysis of the laser intensity distribution on the sample. The FWHM of the laser spot, as measured on a charge-coupled device array, is  $220 \mu\text{m}$ . This leads to a predicted angular width of 2.8 mrad instead of 3.4 mrad. The angular width measured in figure 6 is actually 2.33 mrad, that is to say *smaller* than the most optimistic prediction. The corresponding spectral resolution is  $125 \text{ MHz} \times 2.3/$

Table 1. Main values for the experimental set-up.

Repetition rate	2000 shots/s
Engraving step duration	250 $\mu\text{s}$
Spectral analysis step duration	250 $\mu\text{s}$
FWHM spot diameter	180 $\mu\text{m}$
Beam intensity	
Beam 1	3.4 mW
Beam 2	5.0 mW
Beam 3	1.32 mW
Angular scanning range	86 mrad
Angular speed $\omega$	344 rad s <sup>-1</sup>
Temperature	4 K

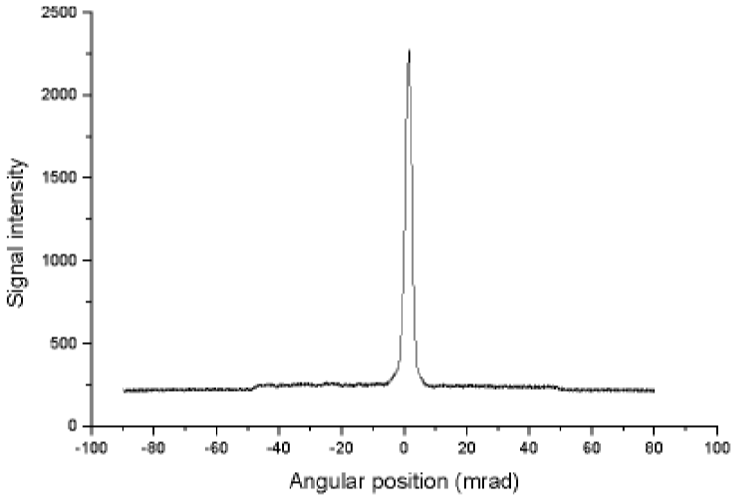


Figure 6. Single-line analysis, with a detection window of 125 MHz bandwidth.

$8.6 = 3.34$  MHz. The laser linewidth is clearly much smaller than this value and does not contribute to the line broadening.

In order to increase the scanning range, we amplify the voltage waveform that is fed to the laser intracavity electro-optic crystal. Unfortunately the accidental breakdown of our only antireflection-coated laser chip prevented us from benefiting from the expected broad-band mode-hop free scanning range of the novel extended-cavity semiconductor laser [13]. The scanning range is thus limited to less than 2.5 GHz by the laser mode interval. The angular linewidth is slightly larger than that observed in the 125 MHz scanning range experiment. It amounts to 3.3 mrad, the scanning range being set to either 1 or 1.5 GHz. We have checked the high-voltage amplifier output noise. It does not exceed 50 mV, which corresponds to a laser frequency shift of 0.6 MHz. This is much smaller than the 57 MHz spectral resolution attained in a 1.5 GHz scanning range experiment. We verified that diffraction efficiency does not significantly depend on the probe pulse temporal position within the readout window 250  $\mu$ s wide. This indicates that engraving is actually accumulated in the long-lifetime shelving state  $^3F_4$  (see figure 3).

Under the assumptions of vanishing laser linewidth and infinite dipole lifetime, the signal spectral width  $\delta\nu$ , as detected on the PDA, is a linear function of  $\bar{\nu}$ , the bandwidth covered by the engraving beams. It is given by  $\delta\nu = \delta\varphi \bar{\nu} / \bar{\varphi}$ , where  $\delta\varphi$  and  $\bar{\varphi}$  represent the angular FWHM of a single line profile and the angular scanning range of the engraving beams respectively. Keeping the engraving time interval and angular scanning range constant, we varied  $\bar{\nu}$  by changing the amplitude of the voltage ramp applied to the intracavity crystal. We measured  $\delta\varphi$  and plotted  $\delta\nu$  as a function of  $\bar{\nu}$  (figure 7). The experimental data depart from the expected linear behaviour for bandwidths smaller than 50 MHz. This can be ascribed to the finite atomic line and laser width. However, the atomic dipole and laser contribution to signal broadening appears to be smaller than 500 kHz. This result apparently indicates that the laser stability has been significantly improved.

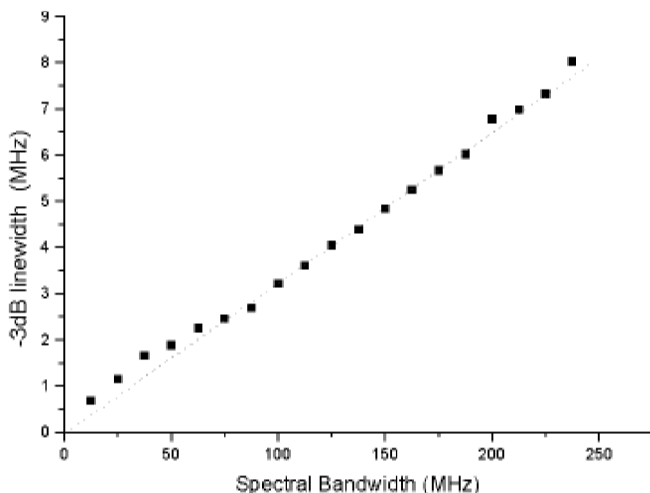


Figure 7. Spectral linewidth as a function of the bandwidth covered by the writing beams. The signal duration is set equal to  $4\mu\text{s}$ . The powers of beams 1, 2 and 3 are measured to be 2.3 mW and 3.35 mW and 0.9 mW respectively.

#### 4.2. Dynamic range

In order to investigate the dynamic range we studied the diffracted intensity as a function of the probe power. The probe power was varied over a range of 3.3 orders of magnitude. The limited dynamic range of the detector did not allow us to exceed a probe power of  $76\mu\text{W}$ , with a gate  $20\mu\text{s}$  wide. The lowest probe power giving rise to a detectable signal on the detector floor noise is  $40\text{nW}$ . Another aspect of the dynamic range is the ability to detect a small signal in the wings of a large one. In the data presented in figure 8, the large signal wings exhibit spurious features that very probably correspond to undesired reflection in the optics. This stray light could be eliminated. In this connection, it should be noted that the pixel size is not adapted to that of the diffracted signal since the pixel height is more than

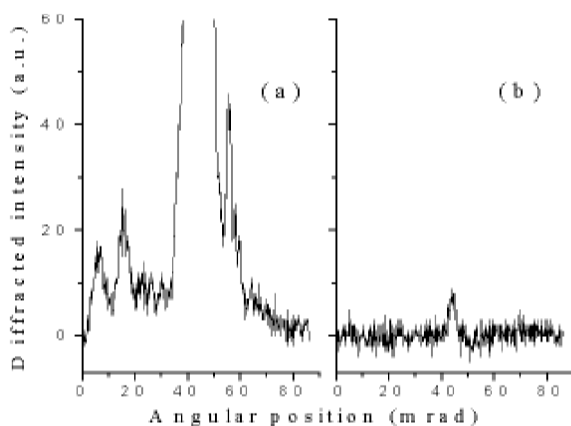


Figure 8. Comparison of (b) a low intensity signal profile and (a) the wings of a high intensity signal. On the same scale the amplitude of the small and large signal are about 12000 and about 10 respectively.

five times the diffracted beam diameter. The full width of the wings of the diffracted signal itself does not exceed 20 mrad. The small signal,  $3 \times 10^4$  less intense than the large signal, could be detected at a distance of about 10 mrad.

#### 4.3. Multiple-line analysis, bandwidth flexibility and spectral zooming

We simulate a multiple line rf signal by making the probe beam achieve a staircase frequency scan during the spectral analysis time interval. A 20-line spectrum has been analysed. The 20 lines cover an interval of 125 MHz (figure 9) or 2.34 GHz (figure 10). The spectrum 125 MHz wide is obtained with good contrast. The spectrum 2.34 GHz wide offers poorer contrast, which is consistent with the poorer angular resolution observed in the single-line spectrum.

The arbitrary connection of the angular and spectral scanning range of the engraving beams enables us to implement a spectral zooming feature. In order to demonstrate this feature we transferred a five-line rf structure on the probe beam, with a line spacing of 12.5 MHz. The angular scanning range of the engraving beams is set at the fixed value of 86 mrad. The spectral scanning range of the engraving beams is varied from 1 GHz down to 125 MHz. The experimental profiles are displayed in figure 11.

In the broadest-bandwidth operation, the resolution is not sufficient to disclose the rf signal structure. The spectral structure is fully resolved when the bandwidth is reduced to 125 MHz. The time required to adjust the bandwidth is limited by the engraved grating lifetime to about 10 ms.

#### 4.4. Spectral coverage

In an initial series of measurement we studied the spectral bandwidth of the material. This was effected in a simple set-up where a single monochromatic grating was engraved and then probed at the same frequency. We measured the diffracted intensity as a function of the laser frequency that was given by a Burleigh 1000 wavemeter. We tuned the extended cavity laser by moving the grating with the help of a piezoelectric mount. The tuning range was limited by the

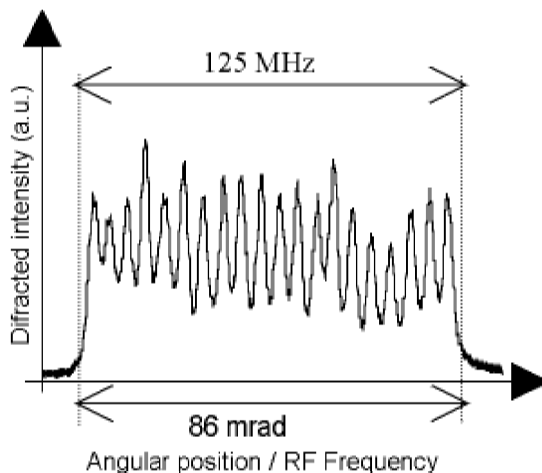


Figure 9. Analysis of a 20-line spectrum covering a 125 MHz interval.

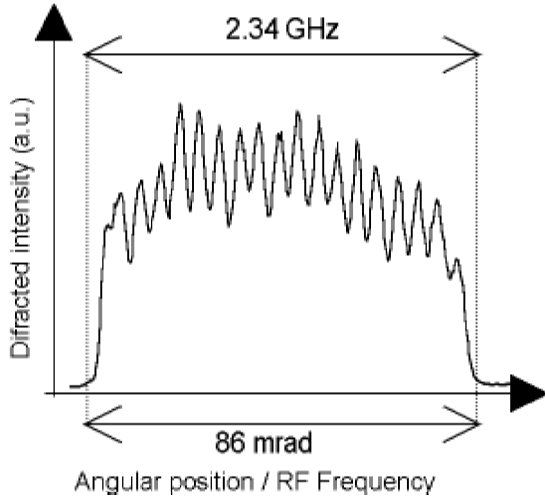


Figure 10. Analysis of a 20-line spectrum covering a 2.34 GHz interval.

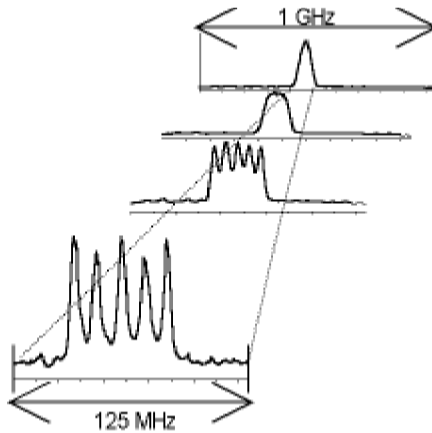


Figure 11. Spectral zooming feature. A signal is first analysed in a broad-bandwidth low-resolution configuration. Then, without changing the angular scanning range, one reduces the scanned bandwidth, which simultaneously improves the spectral resolution. As a consequence the detailed structure of the signal is revealed.

free spectral range of the semiconductor cavity to about 50 GHz. Experimental results are displayed in figure 12. The scanning range does not cover the entire diffraction profile. However, from this measurement we expect a material bandwidth of about 20 GHz at 3 dB attenuation.

### 5. Conclusion

We have demonstrated broad-band SHB spectrometer operation. The expected spectral resolution was reached, which means that we were able to achieve the fast broad-band frequency scan of the laser, with a high degree of repeatability,

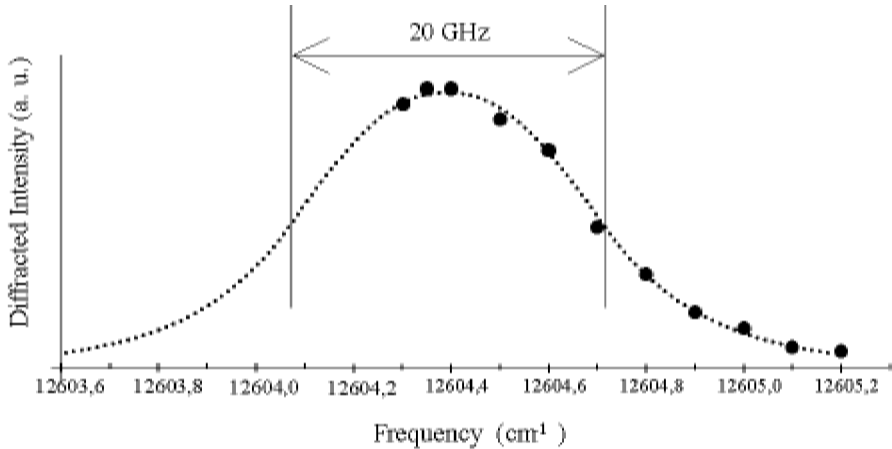


Figure 12. Measured diffracted intensity as a function of the probe frequency (●) and the extrapolated spectral response profile (·····). The explored spectral region was limited by the laser tuning range.

in synchrony with the angular scan of the writing beams. The spectral range limitation to 2.5 GHz is accidental. As soon as we obtain another antireflection-coated laser diode we shall be able to broaden this range. Broader-band operation also demands that one takes care of the crystal heating and that one prepares ions in a stationary excitation state. Both requirements are easily satisfied. The crystal can be cut to dimensions close to the spot size, thus enabling homogeneous cooling to take place through the sides of the crystal. Preparation of the ions population in a stationary excited state is expected to minimize instantaneous spectral diffusion that may spoil spectral resolution. This is satisfied with the repetitive engraving scheme used in the experiments reported here.

In the light of the present results, satisfactory stability conditions can be found, which will open the way to long integration times. Future developments will include the following:

- (i) two-dimensional operation, which is needed to increase the channel number so that broad-band coverage and high resolution can be attained simultaneously;
- (ii) adjustment of the detector pixel size to the diffracted beam angular resolution, in order to optimize sensitivity and minimize stray light;
- (iii) 100% duty cycle operation, for which the probe beam must be provided by a separate fixed-frequency, laser that has to be referenced to the continuously swept writing laser;
- (iv) compact design of the different modules in view of the set-up integration as a laboratory demonstrator.

### Acknowledgments

We are grateful to the European Space Agency for continuing support provided under contracts ESA 12876/98/NL/MV and ESTEC 14174/00/NL/SB. We are

very grateful to Lars Levin and Professor Stefan Kröll who conceived and developed the laser used in these experiments [13].

## References

- [1] MÉNAGER, L., LORGERÉ, I., LE GOUËT, J.-L., DOLFI, D., and HUIGNARD, J.-P., 2001, *Optics Lett.*, **26**, 1245.
- [2] ZHU, M., BABBITT, W. R., and JEFFERSON, C. M., 1995, *Optics Lett.*, **20**, 2514.
- [3] TIAN, M., GRELET, F., LORGERÉ, I., GALAUP, J.-P., and LE GOUËT, J.-L., 1999, *J. Opt. Soc. Am. B*, **20**, 74.
- [4] WANG, T., LIN, H., and MOSSBERG, T. W., 1995, *Optics Lett.*, **20**, 2541.
- [5] HARRIS, T. L., SUN, Y., CONE, R. L., MACFARLANE, R. M., and EQUALL, R. W., 1998, *Optics Lett.*, **23**, 636.
- [6] MERKEL, K. D., and BABBITT, W. R., 1996, *Optics Lett.*, **21**, 1102.
- [7] MOERNER, W. E. (editor), 1988, *Persistent Spectral Hole Burning: Science and Applications* (Berlin: Springer).
- [8] MACFARLANE, R. M., HARRIS, T. L., SUN, Y., CONE, R. L., and EQUALL, R. W., 1997, *Optics Lett.*, **22**, 871.
- [9] EQUALL, R. W., SUN, Y., CONE, R. L., and MACFARLANE, R. M., 1994, *Phys. Rev. Lett.*, **72**, 2179.
- [10] MACFARLANE, R. M., 1993, *Optics Lett.*, **18**, 829.
- [11] HESSELINK, W. H., and WIERSMA, D. A., 1981, *J. chem. Phys.*, **75**, 4192.
- [12] MOSSBERG, T. W., 1982, *Optics Lett.*, **7**, 77.
- [13] MÉNAGER, L., CABARET, L., LORGERÉ, I., and LE GOUËT, J.-L., 2000, *Optics Lett.*, **25**, 1246.
- [14] LEVIN, L., 2002, *Optics Lett.*, **27**, 237.

Copyright of Journal of Modern Optics is the property of Taylor & Francis Ltd and its content may not be copied or emailed to multiple sites or posted to a listserv without the copyright holder's express written permission. However, users may print, download, or email articles for individual use.